Solid State Ionics 193 (2011) 11–17

Contents lists available at ScienceDirect

Solid State Ionics

journal homepage: www.elsevier.com/locate/ssi

Assessment of the electronic conductivity of core–shell, Fe-doped LSGM ceramics by impedance spectroscopy

Eduarda Gomes [a], Glenn C. Mather [b], Filipe M. Figueiredo [c,*], Fernando M.B. Marques [c]

[a] School of Management and Technology, Polytechnic Institute of Viana do Castelo, Avenida do Atlântico, 4900-348 Viana do Castelo, Portugal
[b] Instituto de Cerámica y Vidrio, CSIC, Cantoblanco, 28049 Madrid, Spain
[c] Ceramics and Glass Engineering Department, CICECO, University of Aveiro, 3810-193 Aveiro, Portugal

ARTICLE INFO

Article history:
Received 11 November 2010
Received in revised form 1 March 2011
Accepted 2 March 2011
Available online 19 May 2011

Keywords:
Lanthanum gallate
Mixed conductor
Grain boundary engineering
Impedance spectroscopy
Electronic conductivity

ABSTRACT

The structure, microstructure and low-temperature electrical properties of core–shell-type mixed conductors based on lanthanum gallate with Fe-doped grain boundaries are analyzed in depth. Electron probe microanalysis revealed that the iron concentration in the grain-boundary regions (shell) is below 1 at.% and their thickness is no more than 1.5 μm. The low-temperature (<400 °C) electronic conductivity is enhanced by up to 2–3 orders of magnitude with respect to the corresponding undoped ceramics, as revealed by the analysis of impedance spectra combined with microstructural information. The electronic transport numbers lie in the range between 0.35 and 0.1 at 275 to 400 °C, decreasing at higher temperatures, where the influence of grain boundaries on the overall transport properties vanishes and the ionic conductivity increases.

© 2011 Published by Elsevier B.V.

1. Introduction

Mixed oxide-ionic and electronic conductors are required for various electrochemical applications, including electrode materials for solid oxide fuel cells and permeating membranes for syngas production. Strategies to enhance mixed conduction, either doping electrolytes with mixed-valence cations [1–4] or processing composites with an electrolyte and an electronic conductor [5–11], proved to be of limited effectiveness. The levels of electronic conductivity obtained by compositional excursions are usually modest, and undesirable reaction or development of ion-blocking interfaces is common in the case of composites.

Recently, we have demonstrated the potential of core–shell-type materials, with electronically conductive grain-boundary regions surrounding the grains of solid electrolytes [12–15]. While the concept seems reasonably simple, the choice of appropriate materials is challenging. Previous work recommended the selection of $La_{1-x}Sr_xGa_{1-y}Mg_yO_{3-\delta}$ (LSGM) as base material. The high ionic conductivity of these materials together with the tolerance of the perovskite structure to dopants [16–20] suggested the possibility of smooth changes in composition from the grain boundaries to the grain interior. Iron was selected as a dopant to try to change the grain-boundary performance of LSGM while preserving the bulk ion-conducting behavior. Small Fe additions to these perovskites have a moderate positive influence on the ionic conductivity [20–22]. Furthermore, Fe diffusion via the grain boundaries of LSGM is known to occur much faster than through the bulk, with a difference of orders of magnitude in the corresponding diffusion coefficients [23]. This opens up a new route to process heterogeneous materials by selective diffusion of the dopant along the grain boundaries of dense ceramics. Some other systems and solutions are more suitable. An interesting example is grain-boundary Co-doped ceria for which only 2 at.% localized (grain-boundary) co-doping substantially improved the mixed conductivity [24,25]. Although the ambipolar conductivity of these core–shell heterostructures is insufficient for a technological application, it is the highest yet reported for a fluorite-type structure.

Fig. 1 illustrates the microstructural features and preferential electrical-transport pathways in core–shell mixed conductors. The potential of this type of material is particularly appealing for low-to-intermediate temperature electrochemical devices, when grain boundaries have a higher impact on the overall transport properties.

Here, we complement the analysis of the low-temperature electrical behavior of core–shell Fe-doped LSGM ceramics using electron probe microanalysis and X-ray diffraction to quantify doping at microstructural and structural levels, and assess the local electronic conductivity of these materials.

2. Experimental procedures

Disk-shaped pellets of LSGM samples ($La_{0.95}Sr_{0.05}Ga_{0.90}Mg_{0.10}O_{3-2.925}$) were prepared from oxides and carbonates, after milling, pressing and sintering. One series of samples (abbreviated as LSGMc) with large grain size (*ca.* 10 μm) was prepared following a conventional ceramic route,

* Corresponding author. Tel.: +351 234 401 464; fax: +351 234 425 300.
E-mail address: lebre@ua.pt (F.M. Figueiredo).

0167-2738/$ – see front matter © 2011 Published by Elsevier B.V.
doi:10.1016/j.ssi.2011.03.006

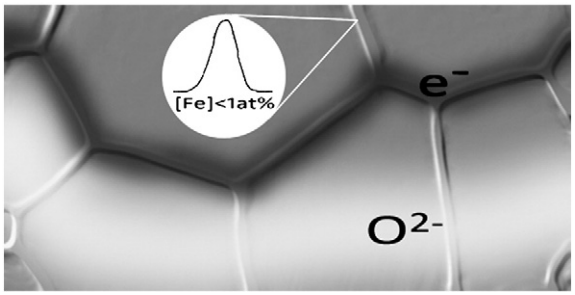

Fig. 1. Schematic representation of the preferential pathways for ionic and electronic transport in grain-boundary-doped, mixed-conducting ceramics. Note the envisaged localized low dopant concentration.

with sintering at 1550 °C for 4 h. Another series of samples (LSGMm), with grain size lower than 0.5 μm, was obtained from mechanically activated precursors, with final sintering at 1450 °C for 4 h. Further details of the preparation and properties of these samples can be found elsewhere [26].

The X-ray diffraction (XRD) patterns of LSGM were obtained at room temperature (Rigaku Geigerflex D/Max - C series diffractometer using Cu Kα radiation, $10° < 2\theta < 110°$, with a step-width of 0.02° and a collection time of 10 s per point). The patterns were indexed in the Imma space group, and the lattice parameters determined by Rietveld refinement using the program FULLPROF [27].

The LSGMc and LSGMm sintered pellets were screen-printed on both surfaces with $LaFeO_{3-\delta}$ layers and annealed in air at 1450 or 1550 °C during several cycles of 1 h to promote the diffusion of Fe along the LSGM grain boundaries. The phase purity and lattice parameters of these samples were analyzed by XRD as described above. The $LaFeO_{3-\delta}$ layers were carefully removed for the subsequent characterization.

Pellets were polished and thermally etched for scanning electron microscopy and energy dispersive spectroscopy analyses (SEM/EDS, Hitachi 4100S microscope with an EDS Röntec detector), with accelerating voltage of 20 kV and beam current ~10 μA. Polished samples (without thermal etching) were analyzed by electron probe microanalysis (EPMA, CAMECA SX-51 Electron Microprobe) using an accelerating voltage of 20 kV and a beam current of 60 nA.

The electrical properties of the ceramic samples were studied by impedance spectroscopy in air at various temperatures. The spectra were collected on disk-shaped samples with the pseudo-4-electrode configuration in the frequency range 20–10^6 Hz with $V_{ac} = 250$ mV (Hewlett Packard 4284A impedance analyser). Platinum electrodes (Engelhard) were painted onto both surfaces of the pellet and fired at 1000 °C for 5 min. The spectra were analyzed using the program ZView (Version 2.6b, 1990–2002, Scribner Associates).

3. Results and discussion

3.1. Structure and microstructure

The XRD analysis confirmed the expected perovskite phase in the doped materials. The only difference are traces of $SrLaGaO_4$ (JCPDS-ICDD PDF#00-024-1208) in the iron-doped, coarse-grained LSGMc. The lattice parameters of both the LSGMc and LSGMm samples remain essentially unaltered on doping (Table 1). The agreement factors R_{wp} and R_B of the Rietveld analysis are also listed in Table 1. These values, particularly R_{wp}, are higher for the doped phase due to the difficulty of fitting the profile shapes. There are several possible reasons for these high R values. It may be that a small, broad contribution to the profiles from crystalline Fe-substituted LSGM perovskite with a different symmetry (e.g. cubic and rhombohedral) along the grain boundaries is responsible for the poor profile fit in the doped cases. Regardless of these or any other possibilities, these results show that the Fe induce minimum (if any) changes in the lattice parameters of the host LSGM lattice.

Table 1
Comparison of the lattice parameters and unit-cell volume for iron-doped and undoped LSGM obtained by conventional solid-state reaction (LSGMc) and mechanical activation (LSGMm).

Material	Lattice parameters/			Unit cell volume/ ^{3}	Agreement factors
	A	*b*	*C*		R_{wp}; R_B (%)
LSGMc undoped	5.4994(2)	7.7966(3)	5.5344(2)	237.30(2)	8.02; 2.78
LSGMc doped at 1550 °C/3 h	5.5014(4)	7.7959(6)	5.5356(4)	237.41(3)	15.3; 6.25
LSGMm undoped	5.4959(2)	7.7894(3)	5.5331(2)	236.87(2)	9.87; 3.98
LSGMm doped at 1450 °C/3 h	5.4953(2)	7.7866(3)	5.5323(2)	236.72(2)	17.1; 12.7

While the formation of $LaSrGaO_4$ in $La_{0.80}Sr_{0.20}Ga_{0.80}Mg_{0.20-x}Fe_xO_{3-\delta}$ has been reported for $Fe \geq 0.05$ [21,28], the nearly invariant unit-cell parameters is coherent with the expected low dopant concentration. The presence of $LaSrGaO_4$ in LSGMc may be due to less homogeneous grain boundaries in the starting ceramics prepared by the ceramic route, usually related to incomplete Mg dissolution [28]. Indeed, some SEM micrographs of thermally etched LSGM samples doped at 1450 °C depict Mg-rich dark precipitates along the grain boundaries which were not present in the undoped materials, thus suggesting that Fe may affect the solubility of Mg cations (Fig. 2). Different diffusivities of La and Fe, resulting in a slight La-excess and eventual possible segregation of secondary La-rich phases, are unlikely since the measured diffusion coefficients of all LSGM cations and Fe (in LSGM) are very similar and coupled La–Fe diffusion is thus to be expected [23]. Nonetheless, $LaSrGaO_4$ is not expected to have a deleterious effect on the grain-boundary ionic conductivity [17].

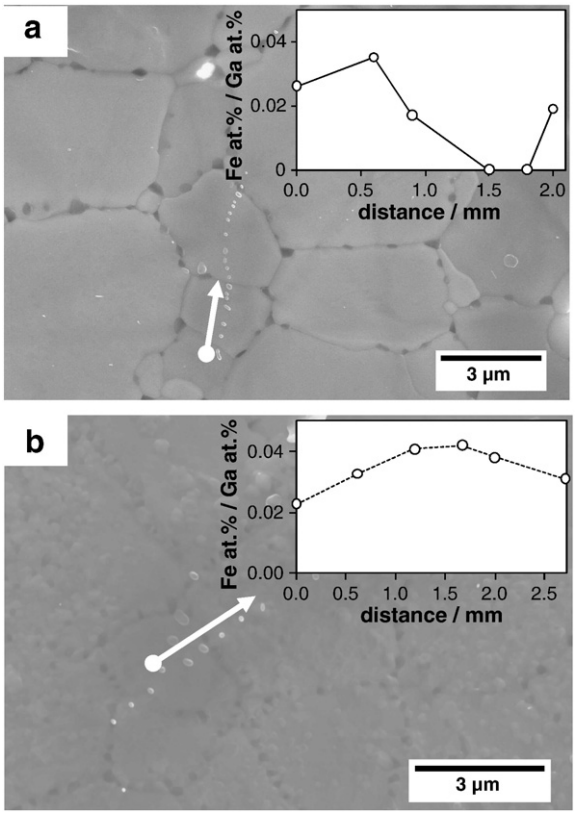

Fig. 2. Typical SEM images of one (a) LSGMc sample after three Fe-doping cycles of 1 h each, at 1450 °C, and one (b) LSGMm doped in the same conditions. Fe/Ga atomic concentration ratio along the arrows shown in (a), (●) across the grain and in (b), (○) across one grain boundary. The white spots near the arrows are the marks left by the electron beam after the EDS analysis.

The SEM analysis of LSGMc pellets impregnated at 1450 °C revealed a microstructure similar to that of the undoped material, with an average grain size of the order of 10 μm (Fig. 2(a)). In contrast, major changes were induced by doping the LSGMm ceramics at 1450 °C, with the grain size increasing from less than 0.5 μm to about 3 μm (Fig. 2(b)). The EDS analysis of the LSGMc ceramics suggests that the thickness of the Fe-doped region does not exceed 1–2 μm (inset in Fig. 2(a)). However, the intensity of the Fe signal is noticeably lower for LSGMm, and the change in the Fe:Ga atomic-ratio profile along the boundary regions is smoother than for LSGMc (insets in Fig. 2). This latter observation may partly result from the limited lateral resolution of EDS (*ca.* 1.4 μm), which is insufficient to resolve compositional differences on the scale of the LSGMm grain size (2–3 μm). Nonetheless, the distinguishable Fe:Ga ratio maximum suggests a thinner (≤1 μm) doped region in comparison to that of LSGMm. These microstructural and compositional aspects are consistent with previous work and represent the current understanding of these systems [12,15].

In order to partly overcome the SEM/EDS resolution limitation and to quantify the iron concentration, the samples were analyzed by EPMA, with lower accelerating voltage and beam current than in SEM/EDS. Fig. 3(a), (b) and (c) depicts the Fe atomic concentration along a line crossing multiple grains, parallel to and near the surface. The interaction volume of the electron beam with a sample under EPMA at 20 kV/60 nA is close to 1 μm^3 whereas the lateral resolution should be slightly in excess of 1 μm. Since the EPMA data were collected at discrete 1 μm-spaced points and most peaks are composed of at least two data points, the thickness of the impregnated regions must be larger than the lateral resolution of the technique. This means that the coincident spacing between Fe-concentration maxima (Fig. 3) and ceramic grain size (Fig. 2) indicates that Fe is predominantly located at the grain boundaries, quantitatively confirming earlier SEM/EDS results [12,15]. The grain-boundary peak Fe concentration (0.5–1.0 at.%) is well above the detection limit (~0.1 Fe at.%), whereas the signal count at the center of the grains is statistically not representative. Obviously, this value is an average for the interaction volume and might mask even more pronounced Fe-concentration peaks in narrower regions, outside the resolution of the technique.

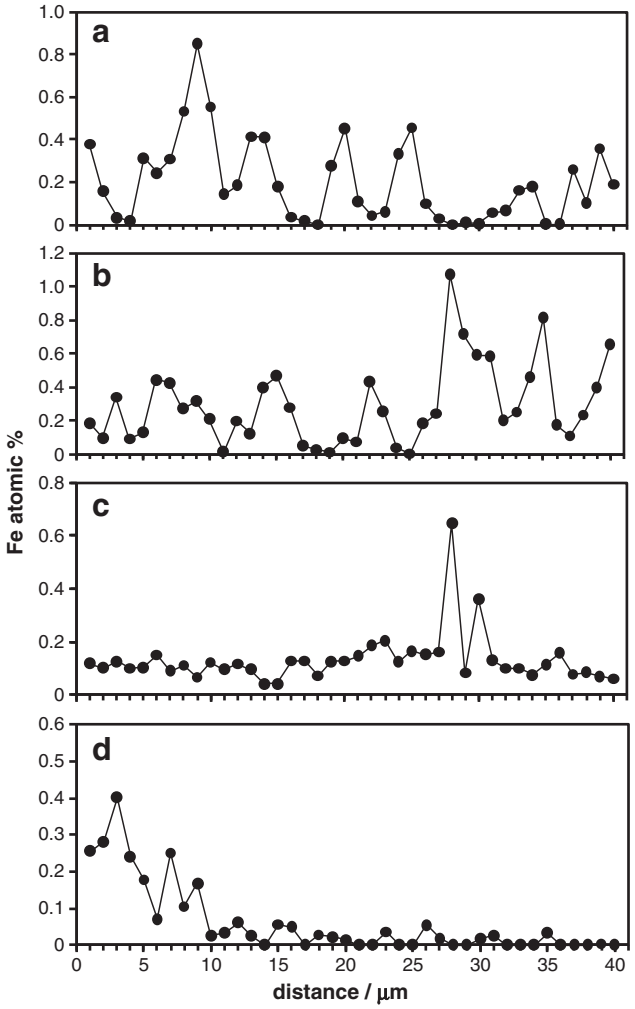

Fig. 3. Iron concentration profiles obtained by EPMA showing multiple maxima interspacing coinciding with the grain size of LSGMc doped at (a) 1550 °C, (b) 1450 °C and (c) LSGMm doped at 1450 °C, and (d) along the transversal length (thickness) of the LSGMc sample doped at 1450 °C. The detection limit is ~0.1 at.%.

The comparison of LSGMc doped at 1450 °C and 1550 °C (Fig. 3(a) and (b)) reveals that both the Fe concentration and width of the doped region are not significantly affected by the doping temperature. However, the former is much lower in the case of the ceramics with smaller grain size, namely LSGMm doped at 1450 °C (Fig. 3(c)). However, the insufficient spatial resolution of EPMA prevents a clear distinction between grain interior and boundary regions in this sample. If the diffusion coefficient of Fe in LSGM is about 6 orders of magnitude larger in the grain boundaries than in the bulk [23,24], as expected for LSGMc and LSGMm, the lower iron concentration in the latter material must result from the considerably longer grain-boundary diffusion pathways in the fine-grained sample.

The particular geometric configuration of the LSGM/$LaFeO_3$ diffusion couple leads to a concentration gradient from the outer impregnated surfaces to the bulk of the pellet, as confirmed by the Fe concentration profile shown in Fig. 3(d). The doped thickness is strongly affected by the annealing conditions, decreasing from nearly 160 μm (80 μm on each side of the pellet) for LSGMc annealed at 1550 °C, to about 30 μm at 1450 °C; this is expected on consideration of the very high activation energies (*ca.* 500 $kJmol^{-1}$ in the upper 900–1400 °C temperature range) reported for the Fe bulk diffusion coefficient in LSGM [23]. Conversely, the doped region of the fine-grained LSGMm doped at 1450 °C is nearly 30 μm thick, which is very close to the value measured for LSGMc doped at the same temperature, although, as mentioned, with lower concentration. It should be added that the impregnation was effective beyond the regions close to the surface of the pellets, as indicated by the dark color through the entire pellet section, even though the low Fe concentration away from the surface is below the experimental detection limit.

An approximate estimate of the total iron concentration in the samples can be obtained from the EPMA results, assuming grains of cubic shape, the pellet dimensions (*L*-thickness and *S*-cross surface area) and the microstructural features, including the grain size, and the thicknesses of the grain-boundary doped regions (Table 2). The density (6.94 gcm^{-3}) was derived from the powder XRD patterns and assumed to be the same for the doped and undoped regions. The estimated Fe concentrations are

Table 2
Geometric, microstructural and EPMA data used to estimate the total iron concentration in the doped materials (3 h at the indicated temperature).

	Material		
	LSGMc (1550 °C)	LSGMc (1450 °C)	LSGMm (1450 °C)
Average grain size/μm	15	10	3
Thickness of doped region in grain/μm	1.5	1.5	1.0
Thickness of doped region in pellet/μm	160	30	30
Thickness of pellet (*L*)/cm	0.145	0.145	0.148
Surface area of electrodes (*S*)/cm^2	0.238	0.233	0.387
Volume fraction of doped regions	5.38	1.36	1.95
Fe at.% in doped regions	0.46	0.46	0.14
Density/gcm^{-3}	6.94	6.94	6.94
Total at. Fe concentration/ppm	246	63	27

in the ppm range and span about an order of magnitude between the more- (LSGMc/1550 °C) and the less-doped (LSGMm/1450 °C) materials.

The good agreement between the EPMA and the powder XRD data (Fig. 2 and Table 1) is notable, both indicating insignificant changes upon doping. This global low-doping approach has positive indirect consequences, since substantial amounts of mixed-valence cations enhance chemical-expansion mismatch when under large oxygen-activity gradients. This frequently leads to mechanical failure, which may be minimized by lowering the transition-metal fraction.

The small structural and global compositional differences induced by localized Fe doping have, however, an impressive effect on the low-temperature electrical properties, which can be reasonably well characterized by impedance spectroscopy.

3.2. Electrical conductivity

Fig. 4 shows the typical impedance spectra collected in air for the LSGM ceramics submitted to multiple Fe impregnation cycles. The spectra of the undoped sample consist of the two usual high- and low-frequency contributions of the bulk and grain-boundary polarizations, respectively. The spectra were thus fitted to an equivalent circuit comprising a series association of two resistors in parallel with constant-phase elements (the top, solid-lined branch in the circuit shown in Fig. 7(a)). The relevant fitting parameters are the bulk and grain-boundary ionic resistances (R_b, R_{gb}), the pseudocapacitances (Q_b, Q_{gb}) and the exponents accounting for the depression of the semicircles (n_b, n_{gb}). Typical fitting results are listed in Table 3 for LSGMc and LSGMm.

The effective capacitances associated with the bulk and grain-boundary phenomena (C_b and C_{gb}) were estimated from these fits by $C=(QR)^{1/n}R^{-1}$, where Q is obtained from the impedance of the constant-phase element $Z_Q=i(\omega^n Q)^{-1}$. The capacitances are nearly temperature independent for the undoped materials (solid symbols and dashed lines in Fig. 5) and of the expected magnitude for polycrystalline LSGM [29,30].

The R_b and R_{gb} resistances were used to obtain the corresponding conductivities from $\sigma_i=R_i\cdot LS^{-1}$, where L is the thickness of the pellet and S is the surface area of the electrodes. The conductivity results are shown in Arrhenius coordinates in Fig. 6. The bulk conductivity (σ_b) is similar for all undoped samples, as expected for materials of the same composition (solid symbols and dashed lines in Fig. 6(a)). The corresponding activation energies are 96–97 kJmol^{-1}. The grain-boundary conductivity (σ_{gb}), however, is higher for the coarse-grained LSGMc, with activation energies of 102–103 kJmol^{-1}. The differences between the various samples are attenuated when comparing the specific grain-boundary conductivity (σ^*_{gb}, estimated by $\sigma^*_{gb}=\sigma_{gb}C_b/C_{gb}$), which, according to the brick-layer model, is independent of microstructural differences. The σ^*_{gb} activation energies are 101 and 107 kJmol^{-1} for LSGMm and the finer LSGMm ceramics, respectively. These differences are indeed small and the data show good agreement with the literature [29].

Table 3
Example of fitting parameters for the impedance spectra of the undoped ceramic samples collected in air at 275 °C.

Fitting parameters		LSGMc (1550 °C)	LSGMm (1450 °C)
Grain interior	R_b/Ω	35,711 (0.16)[a]	20,302 (0.24)
	$Q_b/S.s^n$	8.21×10^{-11} (2.79)	1.07×10^{-10} (6.4)
	n_b	0.89 (0.22)	0.88 (0.49)
Grain boundary	R_{gb}/Ω	6784 (1.21)	14,863 (0.45)
	$Q_{gb}/S.s^n$	8.32×10^{-8} (8.27)	2.68×10^{-8} (2.83)
	n_{gb}	0.85 (1.32)	0.86 (0.40)

[a] Percent fitting errors for each parameter are given inside parentheses.

The impedance spectra of the Fe-doped samples exhibit the two semi-circles of the undoped ceramics. The effect of Fe is a progressive decrease of the amplitude of both arcs with an increasing number of impregnation cycles (Fig. 4). The parallel equivalent-circuit analysis was performed in order to systematize the effects of the dopant on capacitance and conductivity of the bulk and grain boundaries (Figs. 5 and 6). These fits yielded similar C_b values for both doped and undoped materials, whereas C_{gb} tends to increase with increasing dopant concentration (Fig. 5), especially at low temperature.

These differences in C_{gb} may be due exclusively to grain growth. Under this assumption and invoking again the brick-layer model, the σ^*_{gb} values were also estimated (Fig. 6(b)). It can be seen that σ^*_{gb} is considerably higher for the samples with the higher dopant concentration. This suggests an enhancement of the grain-boundary total conductivity beyond that expected from simple grain-size changes. The significant and progressive enhancement of the macroscopic grain-boundary conductivity, σ_{gb}, with increasing dopant concentration cannot be explained by the brick-layer model. It is also apparent from Fig. 6(b) that the improvement of σ_{gb} upon doping decreases with increasing temperature, and the corresponding activation energies of doped samples tend to be lower in the low-temperature range.

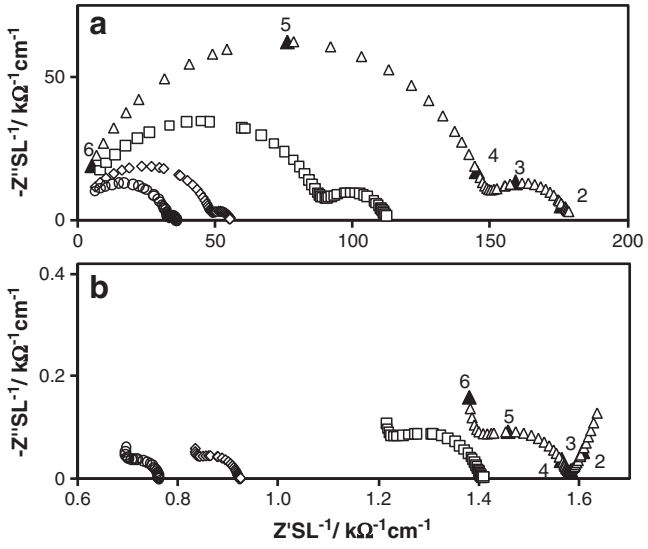

Fig. 4. Impedance spectra collected in air at (a) 300 °C and (b) 400 °C of an LSGMm sample doped at 1550 °C for increasing periods of time: (Δ) undoped, (□) 1 h, (◊) 2 h and (○) 3 h. Numbers indicate $\log_{10}$ of the frequency.

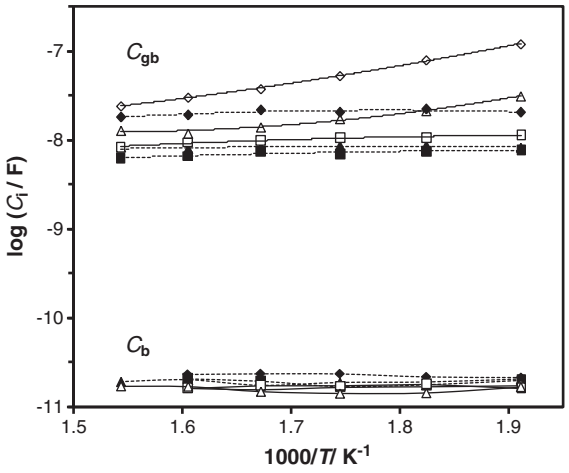

Fig. 5. Bulk (C_b) and grain-boundary (C_{gb}) capacitances for undoped LSGMc (solid symbols, dashed lines) and samples of LSGMc (open symbols, solid lines) doped at 1550 °C (diamonds) and 1450 °C (triangles), and LSGMm doped at 1450 °C (squares). The lines are for visual guidance only.

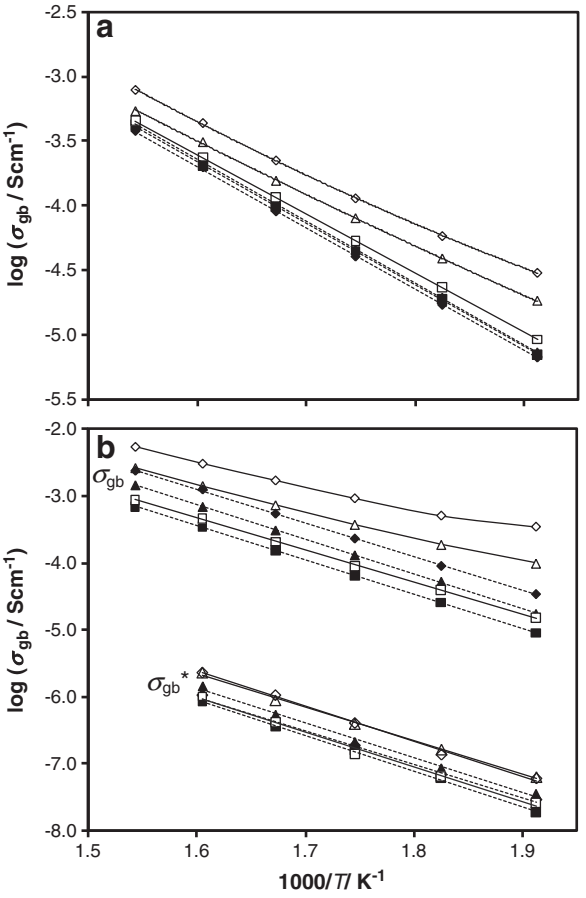

Fig. 6. (a) Bulk (σ_b) and (b) grain-boundary conductivity (σ_{gb} and σ^*_{gb}) for undoped (solid symbols, dashed lines) and Fe-doped (open symbols, solid lines) samples of LSGMc at 1550 °C/3 h (diamonds) and 1450 °C/3 h (triangles), and LSGMm at 1450 °C/3 h (squares).

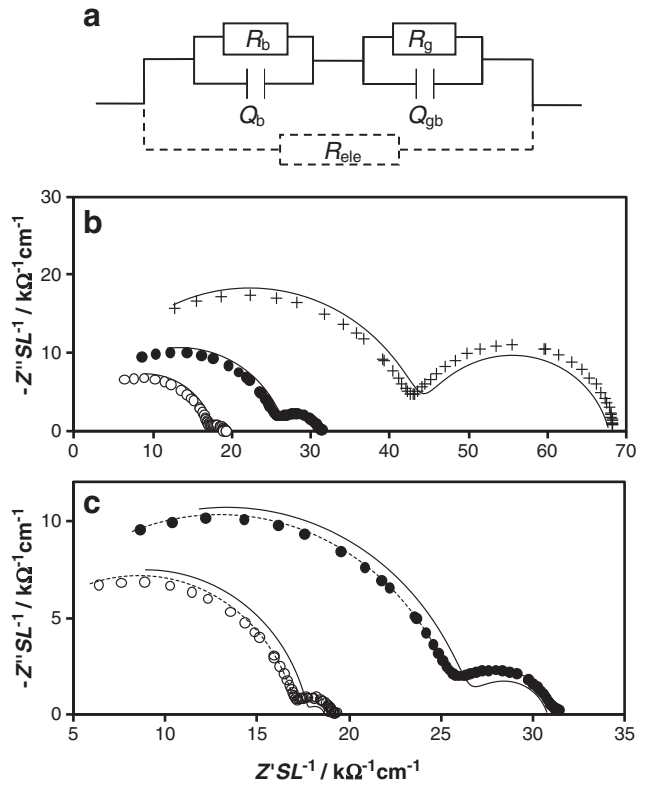

Fig. 7. (a) Equivalent circuit of a polycrystalline ionic conductor with and without electronic conductivity used to fit the (b) impedance spectra collected in air at 275 °C of LSGMc doped at (●) 1550 °C/3 h and (○) 1450 °C/3 h, and (+) LSGMm doped at 1450 °C/3 h. Panel (c) is a zoomed section of (a) showing the best fit to the equivalent-circuit model shown in (a), assuming the parameters of the undoped sample R_j, Q_j, n_j and fitting R_{ele} only (solid lines), or the simultaneous fit of R_{ele}, R_b and Q_b (dashed lines). See text for details.

The effect of doping on σ_b is lower than on σ_{gb} (Fig. 6(a)). For example, at 250 °C, the σ_b of LSGMc doped at 1550 °C increases by a factor of 4.5 (from 6.70×10^{-6} Scm^{-1} to 3.03×10^{-5} Scm^{-1}), whereas there is a 10-fold enhancement in σ_{gb}. Again, the differences between doped and undoped samples become smaller at higher temperature (σ_b increases by a factor of 2 at 375 °C). The increase of the activation energy with increasing temperature is also apparent, with deviation from simple Arrhenius behavior. The enhancement of σ_b upon doping could be due to an increase of the oxide-ionic conductivity. Ishihara et al. reported an approximate 2-fold increase in σ_b at 950 °C for homogeneous $La_{0.8}Sr_{0.20}Ga_{0.80}Mg_{0.17}Fe_{0.03}O_{3-\delta}$ [21,22]. However, this is unlikely in the case of the materials prepared in this work because the Fe concentration in the grain interior does not exceed 0.1 at.%, as demonstrated by EPMA.

3.3. Electronic conductivity

The microstructural and impedance-spectroscopy results strongly suggest that the overall increase in conductivity is mainly due to a conductive electronic pathway along the grain boundaries, in parallel to the grain and grain-boundary oxide-ion paths. This additional electronic pathway is introduced in the initial equivalent circuit model by a parallel electronic resistor (R_{ele}) (Fig. 7(a)) [31]. This equivalent circuit becomes particularly suitable to model heterogeneous mixed conductors assuming that the ionic branch remains essentially unaffected by doping. In these conditions, the bulk (R_b, Q_b, n_b) and grain-boundary (R_{gb}, Q_{gb}, n_{gb}) parameters from the undoped samples are retained, leaving the electronic resistance R_{ele} as the only fitting parameter. Fig. 7(b) shows that the impedance spectra are reasonably well described with this single-parameter model. Fig. 7(c) shows that larger R_b:R_{gb} ratios yield poor fits at the transition between the bulk and grain boundary contributions. There is also a shift of the relaxation frequencies $\omega_0=(RC)^{-1}$ to higher values for the samples with high dopant content, suggesting that either the capacitance, the resistance, or both, may be lower than in the undoped ceramics. Indeed, considerably better fits are obtained by varying R_b and Q_b (with n_b fixed) together with R_{ele}, as shown by the dashed lines in Fig. 7(c). These alternative fits yield slightly higher R_{ele} values, which are compensated by a decrease of R_b or an increase of Q_b. At 275 °C, when the bulk semicircle is better resolved, and for LSGMc doped at 1550 °C (with the higher R_b:R_{gb} ratio), R_{ele} increases from 15,445 Ω, in the case of a single-parameter fit, to 19,821 Ω when fitting simultaneously R_{ele} and Q_b; the latter parameter increases from 8.2×10^{-11} Ss^{-1} to 1.25×10^{-10} Ss^{-1}, and R_b decreases from 35,711 Ω to 21,850 Ω. While the difference in Q_b is within the fitting error, the fact that R_b is almost halved cannot be explained in light of the very low dopant concentration in the interior of the grains. Minor changes in R_b cannot be completely ruled out. However, since the central region of the grains and pellet should behave as pure LSGM, the impedance should be much closer to that of pure LSGM. In the absence, therefore, of a reasonable justification for a variable bulk resistance, the simple fit of R_{ele} is considered to be the most appropriate.

In spite of these limitations, the model provides a reasonably accurate description of the ohmic contributions, as demonstrated in Fig. 8. The excellent agreement between the low-frequency intercept resistance (R_{DC}) and the estimates obtained by $R^*_{DC}=(R_b+R_{gb})R_{ele}/(R_b+R_{gb}+R_{ele})$ [32], is a measure of the goodness of fit for all samples over the temperature range where this was possible.

Fig. 9(a) shows that the estimates of the low-temperature electronic conductivity obtained in this way increase by almost one order of magnitude when the total dopant concentration increases from

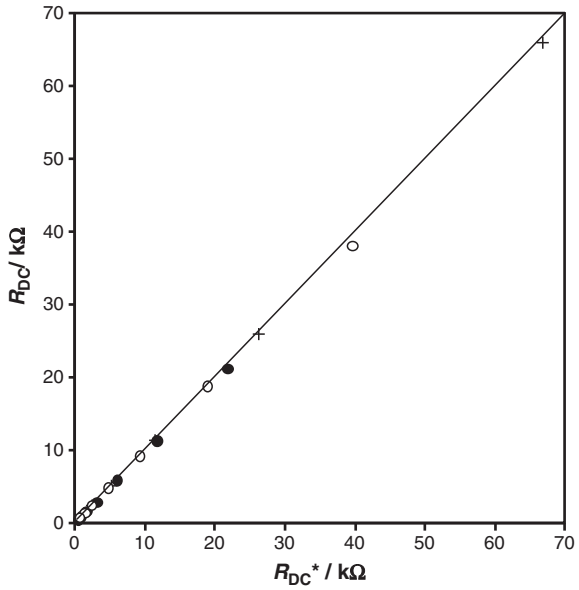

Fig. 8. Comparison of the total resistance, R_{DC} (obtained from the low-frequency intercept of the impedance spectra), with the estimates for R^*_{DC}, depicting a line with a slope of 1 in 250–400 °C temperature range. Symbols correspond to data from samples LSGMc doped at (●) 1550 °C/3 h and (○) 1450 °C/3 h, and (+) LSGMm doped at 1450 °C/3 h. See text for details.

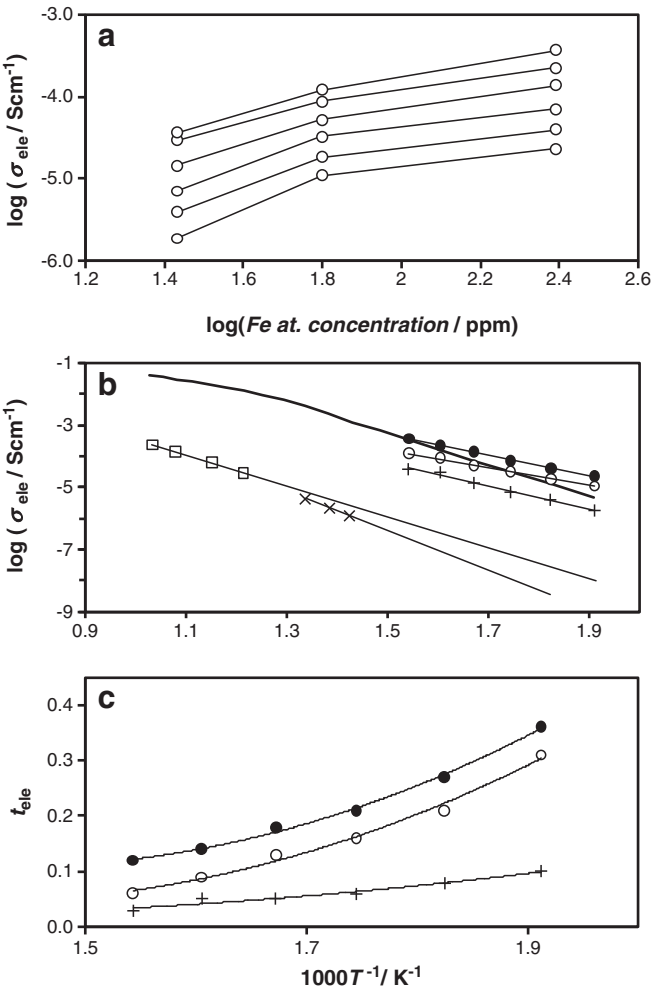

Fig. 9. (a) Electronic conductivity as a function of the total dopant concentration at various temperatures. Data are presented bottom-up from 250 °C to 375 °C in 25 °C steps. (b) Arrhenius plot of the grain-boundary electronic conductivity and (c) electronic transport number of (●) LSGMc doped at 1550 °C/3 h, (○) LSGMc doped at 1450 °C/3 h and (+) LSGMm doped at 1450 °C/3 h. Total conductivity data for $La_{0.95}Sr_{0.05}Ga_{0.90}Mg_{0.10}O_{2.93}$ are shown in (b) as the thick solid line, and σ_{ele} values in (c) for (×) $La_{0.99}Sr_{0.01}GaO_3$ and (□) $La_{0.9}Sr_{0.1}Ga_{0.8}Mg_{0.2}O_{2.85}$ are taken from Refs. [30,33], respectively.

around 30 ppm to 250 ppm. The effect of Fe on σ_{ele} decreases with increasing temperature, as suggested earlier by inspection of the impedance spectra. Nevertheless, this difference in the low temperature range is impressive and illustrates the sensitivity of the material to localized doping. The estimated activation energies for σ_{ele} are 68, 60 and 75 kJmol^{-1} for LSGMc/1550 °C, LSGMc/1450 °C and LSGMm/1450 °C, respectively (Fig. 9(b)). The narrow range of activation energies suggests similar conduction mechanisms for the doped materials. Finally, σ_{ele} estimates are of the same order of magnitude of the ionic conductivity of the undoped material, whereas the activation energy is lower.

To the best of our knowledge, low-temperature grain-boundary σ_{ele} data on the LSGM materials are available only for the lightly Sr-doped material $La_{0.99}Sr_{0.01}GaO_3$ [30]. For compositions similar to the base material $La_{0.95}Sr_{0.05}Ga_{0.90}Mg_{0.10}O_{2.925}$, the available data were obtained at considerably higher temperatures [33,34]. Nevertheless, these values should be two to three orders of magnitude lower than those for the iron-doped materials, as shown in Fig. 9(b). This supports the hypothesis of a strong dependence of σ_{ele} on localized Fe-doping.

The electronic transport number, defined as $t_{ele} = \sigma_{ele}/(\sigma_{gb} + \sigma_b + \sigma_{ele})$, is plotted in Fig. 9(c) and shows that a marked enhancement of the oxide-conducting character is expected at higher temperatures. This behavior is consistent with the high activation energy of the ionic conductivity (Fig. 9(b)) and with the expectation of a decreasing role of grain boundaries with increasing temperature. It is also consistent with the comparatively much smaller dopant effect observed at high temperature, as determined in the 800–1000 °C range by oxygen-permeation measurements [14]. Ishihara and co-workers measured the transport numbers of lightly and homogeneously Fe-doped LSGM ($La_{0.8}Sr_{0.20}Ga_{0.80}Mg_{0.17}Fe_{0.03}O_{3-\delta}$) and observed a similar trend, with the ionic transport number decreasing from nearly unity at 950 °C to about 0.85 at 650 °C [21].

The resistive grain boundaries of $La_{0.99}Sr_{0.01}GaO_3$ can be explained by the depletion of both oxygen vacancies and electron holes and the resulting changes in space-charge distribution [30]. Similarly, in the present case, this may be of particular relevance to the electronic resistance, since the much higher oxygen-vacancy concentration of the Sr and Mg co-doped materials tends to attenuate the magnitude of the space-charge layer. In the case of the electronic conductivity of Fe-doped materials, the number of electron holes introduced with the Fe cations overlaps the space-charge profile, increasing the local electron-hole conductivity. This implies an important fraction of tetravalent iron according to the ionization equilibrium $Fe^{\cdot}_{Ga} \rightleftharpoons Fe^{x}_{Ga} + h^{\cdot}$; the concentration of both species is fixed by $[Fe] = [Fe^{\cdot}_{Ga}] + [Fe^{x}_{Ga}]$. The relatively low grain-boundary activation energy and the appreciable levels of σ_{ele} in the low-temperature range are consistent with the existence of a significant fraction of Fe^{4+} which is confined to the grain-boundary regions. As the temperature increases, the reduction of the Fe^{4+} cations to Fe^{3+} lowers the hole concentration and σ_{ele}. Moreover, the decrease of the Fe^{4+} concentration implies that additional mechanisms are required to form electronic defects, with increasing overall energy requirements.

Although the verification of the existence of tetravalent iron is challenging, considering the low concentration and heterogeneous distribution of the cations, it should be noted that the fraction of Fe^{4+} in homogeneous $La_{1-x}Sr_xGa_{0.7}Fe_{0.2}Mg_{0.1}O_{3-\delta}$ and $LaGa_{0.8-x}Fe_{0.2}Mg_xO_{3-\delta}$ can be as high as 60% at room temperature in air, according to Mössbauer-spectroscopy data [35].

The present results highlight the potential of grain-boundary engineering in developing new types of materials with enhanced performance at moderate temperatures. Nevertheless, the approach

may be particularly demanding from the viewpoint of materials selection and processing to retain the desired microstructures. In fact, there is no single or simple solution for all materials. The degradation of the microstructure and properties during long-term operation at high temperature should be taken into consideration.

While already extraordinary, the improvement of σ_{ele} reported in this work is restricted by the relatively poor distribution of the dopant within the membrane thickness. In thinner samples, however, the potential of the adopted impregnation method is evident and offers considerable flexibility.

4. Conclusions

The combined analysis of microstructure, composition and electrical-transport data of core–shell-structured LSGM with Fe doping of the grain boundaries was used to assess the electronic conductivity of these heterogeneous materials. The low-temperature (<400 °C) total electronic conductivity of LSGM may be enhanced by an impressive 2 to 3 orders of magnitude by localized doping of the grain boundary regions. The effect on electric transport is significantly lower at higher temperature (>800 °C), where only a slight improvement of the electron-hole conductivity could be measured.

Acknowledgments

Financial support from FCT and PRODEP (Portugal), and CEC (Brussels, Network of Excellence FAME) is greatly appreciated. Prof. Derek Sinclair (U. Sheffield, UK) kindly provided open access to EPMA facilities, with the help of Dr. Cathy Shields.

References

[1] B.C.H. Steele, B.E. Powell, P.M.R. Moody, Proc. Br. Ceram. Soc. 10 (1968) 87.
[2] B. Cales, J.F. Baumard, J. Electrochem. Soc. 131 (1983) 2407.
[3] H. Naito, H. Arashi, Solid State Ionics 53–56 (1992) 436.
[4] R.M.C. Marques, F.M.B. Marques, J.R. Frade, Solid State Ionics 73 (1994) 27.
[5] Y. Shen, A. Joshi, M. Liu, K. Krist, Solid State Ionics 72 (1994) 209.
[6] C.S. Chen, B.A. Boukamp, H.J.M. Bouwmeester, G.Z. Cao, H. Kruidhof, A.J.A. Winnubst, A.J. Burggraaf, Solid State Ionics 76 (1995) 23.
[7] J.E. ten Elshof, N.Q. Nguyen, M.W. den Otter, H.J.M. Bouwmeester, J. Electrochem. Soc. 144 (1997) 4361.
[8] V.V. Kharton, A.V. Kovalevsky, A.P. Viskup, F.M. Figueiredo, A.A. Yaremchenko, E.N. Naumovich, F.M.B. Marques, J. Electrochem. Soc. 147 (2000) 2814.
[9] J. Kim, Y.S. Lin, J. Membr. Sci. 167 (2000) 123.
[10] K. Wu, S. Xie, G.S. Jiang, W. Liu, C.S. Chen, J. Membr. Sci. 188 (2001) 189.
[11] U. Nigge, H.-D. Wiemhofer, E.W.J. Romer, H.J.M. Bouwmeester, T.R. Schulte, Solid State Ionics 146 (2002) 163.
[12] E. Gomes, F.M. Figueiredo, F.M.B. Marques, Bol. Soc. Esp. Ceram. V. 45 (2006) 144.
[13] E. Gomes, F.M. Figueiredo, F.M.B. Marques, J. Eur. Ceram. Soc. 26 (2006) 2991.
[14] E. Gomes, F.M.B. Marques, F.M. Figueiredo, Solid State Ionics 179 (2008) 1325.
[15] E. Gomes, F.M. Figueiredo, F.M.B. Marques, Solid State Ionics 179 (2008) 900.
[16] T. Ishihara, H. Matsuda, Y. Takita, J. Am. Chem. Soc. 116 (1994) 3801.
[17] M. Feng, J.B. Goodenough, Eur. J. Solid State Inorg. Chem. 31 (1994) 663.
[18] P. Huang, A. Petric, J. Electrochem. Soc. 143 (1996) 1644.
[19] J.W. Stevenson, T.R. Armstrong, D.E. McGready, L.R. Pederson, W.J. Weber, J. Electrochem. Soc. 144 (1997) 3613.
[20] R.T. Baker, B. Gharbage, F.M.B. Marques, J. Electrochem. Soc. 144 (1997) 3130.
[21] T. Ishihara, T. Shibayama, M. Honda, H. Nishiguchi, Y. Takita, J. Electrochem. Soc. 147 (2000) 1332.
[22] V.V. Kharton, A.P. Viskup, A.A. Yaremchenko, R.T. Baker, B. Gharbage, G.C. Mather, F.M. Figueiredo, E.N. Naumovich, F.M.B. Marques, Solid State Ionics 132 (2000) 119.
[23] O. Schulz, M. Martin, Solid State Ionics 135 (2000) 549.
[24] C. Kleinlogel, M. Goedickmeier, L.J. Gauckler, The Electrochemical Society Proceedings, 99-19, 1999, p. 225.
[25] D.P. Fagg, S. García-Martin, V.V. Kharton, J.R. Frade, Chem. Mater. 21 (2009) 381.
[26] E. Gomes, M. Soares, F.M. Figueiredo, F. Marques, J. Eur. Ceram. Soc. 25 (2005) 2599.
[27] J. Rodriguez-Carvajal, Satellite Meeting on Powder Diffraction, Abstracts of the XVth Conference on the International Union of Crystallography, 1990, p. 127, Toulouse.
[28] A.A. Yaremchenko, A.L. Shaula, D.I. Logvinovich, V.V. Kharton, A.V. Kovalevsky, E.N. Naumovich, J.R. Frade, F.M.B. Marques, Mater. Chem. Phys. 82 (2003) 684.
[29] C. Haavik, E.M. Ottesen, K. Nomura, J.A. Kilner, T. Norby, Solid State Ionics 174 (2004) 233.
[30] H.J. Park, S. Kim, Solid State Ionics 179 (2008) 1329.
[31] J.W. Patterson, in: G. Brubaker, P. Phipps (Eds.), Ionic and Electronic Conduction in Nonmetallic Phases, ACS Symp. Series (No. 89), Corrosion Chemistry, Am. Chem. Soc, Washington, DC, 1979, p. 96.
[32] J. Jamnik, Solid State Ionics 157 (2003) 19.
[33] S. Schmidt, F. Berckemeyer, W. Weppner, Ionics 6 (2000) 139.
[34] J.-H. Kim, H.-I. Yoo, Solid State Ionics 140 (2001) 105.
[35] O. Wakamatsu, M. Yamaguchi, T. Fumoto, T. Hashimoto, A. Kuno, M. Matsuo, Solid State Ionics 179 (2008) 1000.